ELSEVIER

Nuclear Physics A 593 (1995) 463–487

NUCLEAR PHYSICS A

Proton photoproduction from ^{12}C

G.E. Cross [a,1], I.J.D. MacGregor [a], J.C. McGeorge [a], J. Ahrens [b], I. Anthony [a], J.R.M. Annand [a], R. Beck [b], D. Branford [c], T. Davinson [c], P. Grabmayr [d], S.J. Hall [a], P.D. Harty [a], T. Hehl [d], J.D. Kellie [a], T. Lamparter [d], L. Machenil [e], J.A. MacKenzie [c], G.J. Miller [a], R.O. Owens [a], J. Ryckebusch [e], M. Sauer [d], R. Schneider [d], K. Spaeth [d], M. Vanderhaeghen [e]

[a] *Department of Physics and Astronomy, University of Glasgow, Glasgow G12 8QQ, Scotland, UK*

[b] *Institut für Kernphysik, Johannes-Gutenberg Universität, D-55099 Mainz, Germany*

[c] *Department of Physics, University of Edinburgh, Edinburgh EH9 3JZ, Scotland, UK*

[d] *Physikalisches Institut Tübingen, Universität Tübingen, D-72076 Tübingen, Germany*

[e] *Laboratory for Nuclear Physics and Institute for Theoretical Physics, Proefuinstraat 86, B-9000 Gent, Belgium*

Received 17 March 1995; revised 13 June 1995

Abstract

The $^{12}C(\gamma,p)$ differential cross-section in the Δ-resonance region has been measured using tagged photons. Data are presented for 20 MeV wide photon energy bins at 200, 300, 400 and 500 MeV and for proton angles from 52° to 128°. The present $^{12}C(\gamma,p)$ measurements are compared with previous experiments carried out at Frascati, Tokyo and Bonn. Comparisons are also made with theoretical calculations developed at Gent and Valencia which provide an interpretation of the photon reaction mechanism in terms of the major contributing processes. Coincidence data with correlated neutrons, protons and pions are also presented.

Keywords:
PACS: PACS numbers: 25.20.Lj, 27.20.+n

1. Introduction

It has long been realised that in light nuclei, between the giant resonance and the Δ-resonance, photon absorption on correlated proton–neutron pairs is the dominant reaction

[1] Present address: Psion plc, London, England.

SSDI 0375-9474(95)00318-5

mechanism. Detailed tagged photon measurements of the (γ,pn) reaction [1–4] at photon energies $\sim$ 100 MeV have shown that this reaction channel is well described by the quasideuteron (QD) mechanism in which the initial photon absorption is on a proton–neutron pair with the rest of the target nucleus acting as a spectator.

The QD process extends into the Δ-resonance region, but above the pion threshold quasifree pion production (QFπ) processes become dominant. Evidence of both mechanisms is seen in the shapes of the single-arm (γ,p) differential cross sections measured at Bonn [5,6], Tokyo [7–9] and Frascati [10] in the Δ-resonance region. The Bonn measurements [6] show that the (γ,p) cross section is proportional to $Z^{1.15}$. This is explained by the increasing probability in heavier nuclei of final state interactions (FSI), in which pions from initial QFπ processes are reabsorbed on nucleon pairs, leading to the ejection of additional protons. In heavier nuclei [6] the shapes of the measured proton energy spectra show little sign of the characteristic QD strength seen at high proton energies in light nuclei. This can again be attributed to the increasing importance of FSI.

The data reported here are the first results of the analysis of a series of (γ,NN) and (γ,Nπ) experiments carried out on light nuclei using the Glasgow tagged-photon spectrometer [11] at the Mainz 855 MeV electron microtron MAMI [12]. These experiments aim to measure the strengths and detailed properties of the main competing QD and QFπ processes in the Δ-resonance region under a wide range of kinematic conditions. In the present paper proton energy spectra are presented for the ^{12}C(γ,p) reaction for four photon energies which span the Δ-resonance: 200, 300, 400 and 500 MeV. Coincidence (γ,pn), (γ,pp) and (γ,pπ) data provide further insight into the main contributing reaction mechanisms. The present data have a wider energy range and angular coverage than the previous data from Bonn, Tokyo and Frascati. Comparisons are made with the previous data in the regions of overlap.

The present data are also compared with two recent theoretical treatments, developed at Valencia [13,14] and Gent [15–17], which use different methods to calculate photonuclear cross sections. In both cases the theoretical calculations take account of the acceptances of the present experimental detector systems, allowing a direct comparison between two current theories and the present experimental measurements. This avoids the somewhat less satisfactory procedure of the previous work [1–4] in which elementary models were employed to extrapolate the measured cross sections to regions of phase space not covered by the detectors, before comparisons were made with theoretical estimates of total angle integrated cross sections.

2. Experiment and data analysis

2.1. Experimental equipment

Fig. 1 shows the arrangement of the experimental equipment. A 15–20 nA electron beam incident on a 4 μm (3×10^{-4} radiation lengths) nickel foil radiator produced

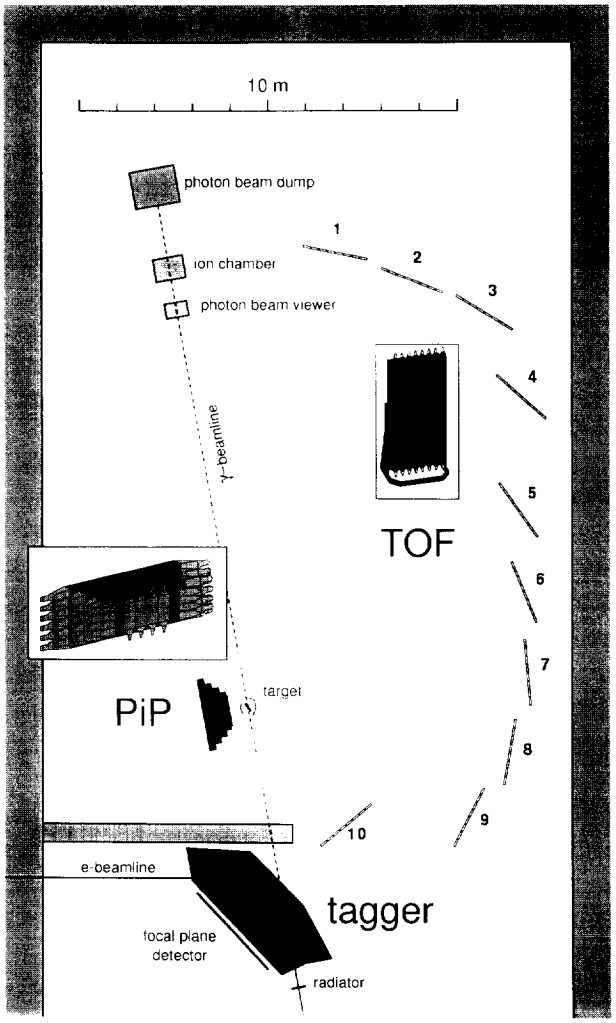

Fig. 1. Schematic arrangement of the experimental apparatus.

bremsstrahlung photons, which were tagged in the Glasgow photon spectrometer [11]. The photon energy resolution was ~ 2 MeV and the total photon flux, over the 114 to 792 MeV tagged photon energy range, was $\sim 5 \times 10^8$ s^{-1}.

The photon beam was collimated to a radius of ~ 8 mm on target, resulting in a tagging efficiency $\varepsilon_t \sim 45\%$. This was measured in a series of separate measurements with a reduced beam current (~ 1 pA) using a 100% efficient Pb-glass detector placed in the photon beam. An on-line indication of the stability of ε_t was provided by the ratio of current in an ion chamber placed in the photon beam downstream of the target to the electron rate in the spectrometer focal plane detector. If this ratio decreased significantly the beam was realigned. A photon beam viewer, mounted in front of the

Table 1
Geometry of PiP detector angular bins

Proton angular bin	Polar angular range (°)	Solid angle (msr)
1	52.3–69.2	200
2	69.2–90.7	287
3	90.7–112.0	283
4	112.0–128.5	194
total	52.3–128.5	964

ion chamber, allowed continuous inspection of the photon beam alignment throughout the measurement. It consisted of a BC430 plastic scintillator screen, viewed by a high sensitivity camera equipped with an image intensifier coupled to an intelligent frame store which allowed the image to be averaged over several frames.

The measurements were carried out using a 261 ± 2 mg/cm^2 graphite target mounted at 30° to the photon beam. For energy calibration a 216 ± 2 mg/cm^2 CD_2 target was used. Separate measurements with the ^{12}C target removed were made to determine the background arising from photon interactions in the air around the target.

Protons were detected in the 6-layer scintillator telescope PiP and associated particles were detected in the time-of-flight array TOF. Preliminary descriptions of these detectors have already been published [18,19] and full reports are presently being prepared for publication. The proton detector PiP, used to determine the energies and emission angles of protons produced in the target, is an expanded version of a smaller segmented scintillation detector array used at lower energies [20]. It has two thin ΔE layers followed by four thick E-layers. The first PiP ΔE scintillator is 150 mm × 100 mm × 1 mm thick, curved in an arc of radius 80 mm with the target at its centre. The signals from this detector were used primarily to indicate the start time for the reaction. The curved shape minimises the variation of path length in the scintillator with particle angle and gives the optimum on-line energy-loss resolution.

The second ΔE layer consists of 4 strips of scintillator each 200 mm wide × 420 mm long × 2 mm thick mounted vertically in a plane ~ 500 mm from the target. This layer defined the total solid angle of 964 msr (see Table 1). The angular acceptance was ~ 77° in the horizontal plane and ~ 44° in the vertical plane. The second ΔE layer was used in conjunction with the two subsequent E-layers for particle identification and it determined the vertical proton position from the time difference between signals from both ends of the element which fired.

The main volume of PiP is divided into four thick layers of horizontal scintillator blocks. The first layer has four blocks each 135 mm × 110 mm × 1 m long and the four second layer blocks are 175 mm × 175 mm × 1.3 m long. The first layer determined the horizontal proton position from time difference measurements. The first and second layers were used to determine proton energies from pulse amplitude information. These two layers stopped protons of energies ~ 210 MeV at central angles and ~ 230 MeV at forward and backward angles. Very few protons had sufficient energy to give signals

Table 2
Geometry of TOF detectors

TOF stand	Mean polar angle (°)	Distance from target (m)	Solid angle (msr)
1	21.0	12.27	31.52
2	31.1	12.13	32.28
3	40.9	12.20	31.91
4	51.3	10.97	39.40
5	63.8	8.87	59.86
6	77.3	7.92	74.72
7	92.8	7.46	83.87
8	109.5	7.02	94.33
9	126.4	6.52	108.88
10	150.2	4.04	267.80

in either of the remaining two layers and given the large energy losses suffered by high energy protons in inelastic nuclear collisions in the scintillator, the signals from these two layers were not analysed. A correction for collision losses, for the lower energy protons stopped in the first two E-layers, was made to the data as described in the next subsection.

Associated particles were detected in TOF [19], an array of plastic scintillator time-of-flight detectors of dimensions $200 \times 50 \times 3000$ mm long mounted vertically in groups of 8. In the present analysis 10 stands, shown in Fig. 1 and Table 2, containing 80 detector elements were used. A 3-segment 2 mm thick plastic scintillator ΔE detector mounted $\sim$ 100 mm from the target was used to discriminate between charged and neutral particles on the TOF side.

The experimental trigger required a triple coincidence between signals from the two PiP ΔE layers and the first E-layer. A threshold set on the sum of pulse amplitude signals from the ΔE layers and the first E-layer rejected most of the background electrons produced in the target. A bypass for events which fired the second E-layer was included to ensure that no high energy particles, which give low pulse amplitudes in the ΔE layers, were lost. A further condition demanded a coincidence with a signal from the tagged photon spectrometer and for some runs a hit in the TOF detectors was also required.

The data acquisition process "ACQU" [21] was run on a VME-bus microcomputer which was linked by ethernet to a VAX workstation. This process controlled the data readout from FASTBUS and CAMAC QDC, TDC and scaler modules and the data transfer. Dead time effects were automatically accounted for as the trigger electronics and the tagger focal plane scalers, which monitored the photon flux, were both gated off by an event latch while each event was processed.

2.2. Proton detection

The position calibration of PiP was obtained as described in Ref. [20] by taking coincidences between each of the first E-layer blocks and the preceding ΔE strips. Linear functions of time difference were obtained for both the horizontal and vertical position calibrations.

The energy loss of particles in the PiP E-blocks is derived from the amplitude of the scintillation light which they produce. This was obtained from the geometric mean of the signals from both ends of each block which largely removed the effects of light attenuation along the scintillator blocks. The residual droop ($\sim 3\%$ in the centre) was corrected using a parabolic function of position. Deuterium two body photodisintegration data, obtained using a CD_2 target, were used to calibrate the energy response of PiP. The procedure used was similar to that described in Ref. [20]. A first analysis indicated that the proton energy resolution was better than ~ 3.3 MeV FWHM at 60 MeV. The proton energy thresholds were ~ 18 MeV for signals in the first E-layer which resulted in effective energy thresholds, after including energy losses before the first E-layer, of ~ 30–35 MeV (depending on angle) for protons originating at the centre of the target.

The response of the scintillator to monoenergetic protons is a peak with a low energy tail due to nuclear reactions in the scintillator material. This process has been studied by Measday and Richard-Serre [22] who showed that $\sim 10\%$ of protons give degraded light output signals at 100 MeV. This rises to $\sim 31\%$ at 230 MeV (the highest energy protons detected in the present work). A correction for the effect of inelastic collisions on the proton spectra was obtained from a model calculation which assumes that protons which have lost energy are redistributed to lower energies with a triangular distribution which increases linearly from zero energy to a maximum at the original proton energy. Those protons which lose less than 35 MeV were then added to the final spectrum; protons which lose more energy were excluded by the particle identification cuts. The size of the correction to the measured spectrum at each proton energy depended on the shape of the spectrum. It was found that for all of the present spectra the yields were small at the highest proton energies where the corrections were largest and large at low proton energies where the corrections were small. The overall distortion of the spectra was therefore small in absolute magnitude at all proton energies, and one set of correction factors was found to be sufficient for all the measured proton energy spectra.

2.3. Detection of coincident particles

As the TOF detectors were only used to identify coincident particles for the work reported in this paper, no detailed calibrations were required. However a rough time calibration was needed in order to select prompt and random coincident events. This was obtained by aligning the easily observed gamma-peak in each TOF detector, and correcting for the distance from the target to each detector to obtain the reaction time-zero (at which particles in prompt coincidence leave the target).

The software pulse amplitude thresholds used in the analysis of data from the TOF detectors were 1 MeV_{ee} (1 MeV equivalent electron energy) for charged particles, and 4 MeV_{ee} for neutrons. The uncertainties in these values were estimated to be ± 0.5 MeV_{ee}. For neutrons this corresponded to a low energy threshold of 8.4 ± 0.7 MeV. The coincident (γ,pn) data presented below were obtained by integrating over all neutron energies above the threshold. The STANTON code [23] was used to calculate the neutron detection efficiency ε_n. It was found that ε_n had a very weak dependence on neutron energy, except for neutrons of energy below $\sim$ 15 MeV. An average energy-weighted efficiency $\varepsilon_n = 6.6\%$, was used in the analysis of all of the (γ,pn) data.

The threshold energies for charged particles were determined principally by the energy losses of each particle between the target and the TOF detectors. This varied considerably as each group of detectors were placed at a different distance from the target. The average energy threshold was $\sim$ 35 MeV for protons and $\sim$ 15 MeV for charged pions.

The effect of pions decaying in flight was considered and for the present purpose it was not considered worth while to make a detailed correction. The fraction of pions which decay over the average flight path of 7.0 m varies from $\sim$ 25% at the highest pion energies to $\sim$ 80% at the lowest pion energies detected. However those pions which decay produce energetic muons with angles less than 35° from the original pion direction at the lowest energies and less than 15° at the highest energies. Muons which still reach the TOF detector array produce signals in the same pulse amplitude versus time-of-flight region as pions, and are therefore identified as pions. Although some pions are lost from the solid angles of the TOF detectors, the effect on the measured (γ,pπ) yield is small, since those pions which are lost are compensated by a similar number gained from neighbouring pion angles.

2.4. Data analysis

The first step was the selection of events in which a proton was stopped in the first two E-layers of PiP. Proton regions, for particles which stopped in the first E-layer, were identified in plots of the pulse amplitude in the second ΔE layer versus that in the first E-layer. Higher energy protons were identified using plots of the pulse amplitude signals in the first E-layer versus that in the second E-layer. The method of particle selection rejected some protons which passed through more than one block in either the first or the second E-layers and deposited only part of their energy in each block. This effect was modelled and a proton-energy-dependent correction factor (of magnitude $\sim$ 3%) was applied to the measured differential cross sections to account for these losses.

For the coincidence data, further particle selections were made using the TOF detector signals. Charged particles were identified by signals from the TOF-side ΔE detector. A plot of TOF pulse amplitude versus time-of-flight then discriminated between protons and deuterons, although the pion locus overlapped with that of protons of energy greater than $\sim$ 230 MeV. However, as very few protons had such large energies, the effect on both the (γ,pp) and (γ,pπ) yields was very small and no corrections were made for it.

Table 3
Systematic errors

Systematic error	Uncertainty (%)
Tagging efficiency ε_t	3
Proton detection efficiency	3
Proton solid angle	2
Number of target nuclei	1
Neutron detection efficiency	10
Effect of uncertainty in TOF thresholds	5

The subtraction of random and target-out events from the final proton energy spectra was carried out as described in Ref. [3]. At the electron beam current used in this experiment, the prompt/random ratio for coincidences between the event trigger and a single tagger focal plane detector channel averaged $\sim$ 1.4. For the coincident reaction channels account was also taken of random hits in the TOF detectors. For charged particles in TOF the fraction of randoms was <5%. For uncharged particles there was a large background of random low-pulse-amplitude signals, but the 4 MeV_{ee} software threshold used reduced the random fraction to $\sim$ 6%. The target-out contribution was found to be less than 5%.

The differential cross sections shown in Figs. 2–11 have error bars which represent the statistical uncertainties in the yields. The uncertainties in the normalisation factors common to all the spectra are not shown. The largest of these are listed in Table 3. The total systematic uncertainty was estimated to be $\sim$ 5% for the (γ,p), (γ,pp) and (γ,pπ) measurements. The total systematic uncertainty of $\sim$ 12% for the (γ,pn) measurements was dominated by the uncertainty in the neutron detection efficiency.

As a check on the overall normalisation of the cross sections, ^{2}H(γ,p) and ^{2}H(γ,pn) data were used to obtain deuterium photodisintegration cross sections between 50 and 400 MeV. The results agreed within errors with the parameterisations of the deuterium cross section by Rossi et al. [24] and Jenkins et al. [25].

3. Results and discussion

Data are presented for the single-arm ^{12}C(γ,p) reaction and for the coincident (γ,pn), (γ,pp) and (γ,pπ) reaction channels, at photon energies of 200 $\pm$ 10, 300 $\pm$ 10, 400 $\pm$ 10 and 500 $\pm$ 10 MeV. For the single-arm data double differential cross sections $d^2\sigma/d\Omega_p dT_p$ have been extracted at each photon energy for proton angular bins at 61$\pm$8°, 80$\pm$11°, 101$\pm$11° and 120$\pm$8°. The same differential cross sections have also been extracted for the coincidence data with the further condition that a neutron, proton or pion is detected in the TOF array. The data show clear signatures of both QD and QFπ mechanisms, as expected from previous work. A detailed analysis is given in the following subsections.

3.1. Comparison with previous experiments

The present data are compared where possible to previous measurements [5,6,9,10]. These earlier experiments also used tagged photon beams, with the exception of the Frascati work [10] which employed a positron annihilation source. These comparisons are fairly limited, as none of the previous $^{12}C(\gamma,p)$ measurements covered as large a photon energy or angular range as the present experiment. Furthermore, there is a limited set of coincidence measurements with which to compare the present work.

3.1.1. Single-arm (γ,p) data

Fig. 2 compares the present $^{12}C(\gamma,p)$ data at $E_\gamma \sim 200$ and ~ 400 MeV with previous data from Frascati, Bonn and Tokyo. The previous data were obtained at slightly different photon energies and proton angles as noted in the figure caption. At the lower photon energy the present data agree reasonably well with the $\theta_p \sim 100°$ Frascati data, except at the lowest proton energies, and the agreement with the Bonn data is also fairly good at this angle. However at forward angles, even allowing for the small differences in photon energy and proton angle, the difference between the present results and the Bonn measurements is large.

At $E_\gamma \sim 400$ MeV, the Tokyo data lie somewhat below the present data and the discrepancies cannot be explained by the differences in energy and angle. However the larger disagreement is again with the Bonn data. At the forward angle this is the case for both the data sets from Bonn, although the shape of the 1980 Bonn data is similar to the present data. At $\theta_p \sim 125°$ the discrepancy in magnitude with the 1980 Bonn data is less, but still significant, even though its shape is similar to the present data.

3.1.2. Coincidence data

The 1980 Bonn coincidence data [5] are averaged over photon energies 315–350 MeV, which provide a rather poor comparison with the present analysis. However the 1991 Bonn data [6] are more extensive and allow comparisons at reasonably close photon energies. Unfortunately no coincident measurements were made for ^{12}C. Instead an ^{16}O target was used so that the following comparisons rely on calculating suitable normalisation factors.

The Bonn experiment detected coincident particles in a time-of-flight detector covering $\sim 10°$–$140°$, which is similar to the present detector geometry. There is, however, a large difference in the azimuthal acceptance of the two detector systems. The Bonn time-of-flight detector had an azimuthal opening angle of $\sim 15°$ which roughly matched their proton spectrometer azimuthal acceptance. In contrast, the present data have TOF azimuthal opening angles of between 14° and 23°, which is less than half the PiP azimuthal acceptance. The present detector arrangement therefore has a lower efficiency for detecting coincident particles which have a strong back-to-back angular correlation.

Correction factors, which account for the different detector acceptances and for the differences in the photon absorption processes and FSI between ^{16}O and ^{12}C were calcu-

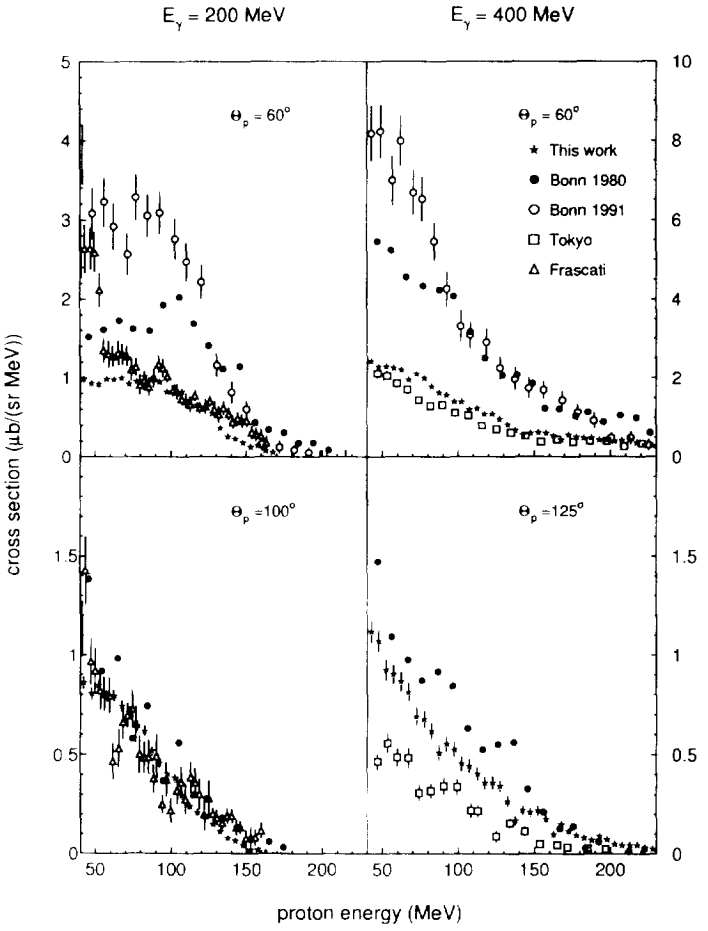

Fig. 2. The $^{12}C(\gamma,p)$ differential cross section as a function of proton energy compared with previous measurements at Frascati [10], Bonn 1980 [5], Bonn 1991 [6] and Tokyo [9]. The E_γ and θ_p ranges of the previous data are: Frascati, $E_\gamma = 198 \pm 3$ MeV, $\theta_p = 55°$ and $\theta_p = 105°$; Bonn 1980, $E_\gamma = 211$ MeV, $\theta_p = 49 \pm 5°$ and $\theta_p = 105 \pm 5°$ and $E_\gamma = 380$ MeV, $\theta_p = 49 \pm 5°$ and $\theta_p = 125 \pm 5°$; Bonn 1991, $E_\gamma = 227$ and 390 MeV, $\theta_p = 52 \pm 6°$; Tokyo, $E_\gamma = 380 \pm 7$ MeV, $\theta_p = 55°$ and $\theta_p = 130°$.

lated using the code developed by Carrasco and Oset, described in the next subsection. These factors were obtained from the ratio of the calculated yields into the Bonn and the present geometries for each of the (γ,pn), (γ,pp) and $(\gamma,p\pi^{\pm})$ reactions. The correction factors obtained (~ 3.2) were similar at $E_\gamma = 300$ and 400 MeV and did not vary significantly with proton energy. The variation amongst the three coincident reaction channels was also small.

Fig. 3 shows the comparison between the Bonn differential cross sections and the present data, multiplied by the calculated correction factors, for the (γ,pn), (γ,pp) and $(\gamma,p\pi)$ reactions at $E_\gamma \sim 300$ and ~ 400 MeV. Overall the present data are in reasonable agreement with the Bonn coincidence data. Although some minor differences

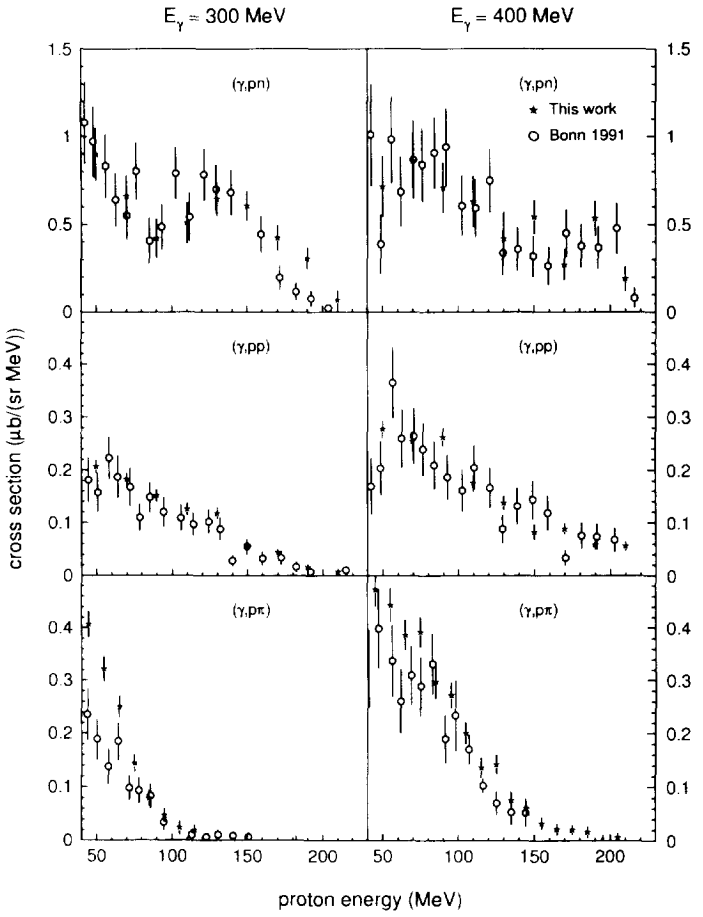

Fig. 3. Differential cross sections for the ^{16}O coincidence data from Bonn 1991 [6] at $E_\gamma = 281$ and 390 MeV and $\theta_p = 52 \pm 6°$ compared to the present ^{12}C coincidence data which have been rescaled, as described in the text, to account for the differences in targets and detector acceptances.

are evident, they are very much less than those observed in the comparison of the inclusive ^{12}C(γ,p) cross sections with the 1991 Bonn study. The reason for this is not understood.

3.2. *Comparison with the Valencia model*

A theoretical interpretation is provided by comparison of the experimental data with calculations carried out using the microscopic model developed by Carrasco and Oset [13,14]. The Valencia model uses microscopic quantum mechanical treatments of the initial photon absorption processes including quasielastic pion production and photon absorption on clusters of two or three nucleons. The emission of two or more nucleons is classified either as "direct" or "indirect"; "direct" production is a single-step process

in which the photon is absorbed on two or more nucleons via the exchange of virtual pions, and "indirect" production is a two-step process in which a photo-produced pion is later reabsorbed on two further nucleons. The subsequent propagation, scattering and reabsorption of nucleons and pions are modelled using a semi-classical Monte Carlo treatment based on local nucleon densities and an optical nucleon–nucleus potential.

The calculation uses a simple Fermi gas treatment of the target nucleus. The initial momenta of the nucleons are obtained by sampling the Fermi distribution and the nucleon binding energies are calculated from their momenta assuming that nucleons at the top of the Fermi sea have zero binding. No other allowance is made for nucleon binding or binding energy differences between the target and residual nuclei, although the energy needed to create pions is taken into account in the treatment of the photon absorption. As a result the predicted missing energy distributions for all reaction channels start at 0 MeV and the average missing energy values are necessarily lower than those observed experimentally [26]. In order to account better for nucleon binding, an energy of 8.4 MeV has been subtracted from the final energy of each emitted nucleon in the output file from the Valencia code. The magnitude of this correction was chosen to bring the average calculated missing energy for 2N photon absorption events, which do not suffer any FSI, into agreement with the average $^{12}C(\gamma,pn)$ missing energy calculated by folding together two single nucleon knockout missing energy spectra as described by McGeorge et al. [4]. This value is also in line with average nucleon separation energies. The effect of this correction on the calculated spectra was small, but it consistently provided a closer agreement with the experimental data.

The Monte Carlo treatment allows each event to be labelled according to the initial photon interaction mechanism. This in turn allows the contributions to each measured reaction channel from different initial photon interaction processes to be identified, even if subsequently some of the particles are subject to secondary rescattering or absorption processes. The total cross sections obtained are an incoherent sum of the contributions from each mechanism. The calculations carried out include the effects of the geometrical and energy acceptances of the present detectors.

3.2.1. The $^{12}C(\gamma,p)$ reaction

The calculations are compared to the measured $^{12}C(\gamma,p)$ differential cross sections in Figs. 4 and 5 for all 16 photon energy and proton angle combinations. The experimental spectra have shapes similar to those established by the earlier (γ,p) experiments which were characterised at the most forward angles [7,8] by a generally falling proton energy spectrum, attributed to QFπ processes, with additional strength at higher proton energies, attributed to 2N processes.

The calculations predict substantial strength for both the $(\gamma,\pi N)$ and 2N photon absorption mechanisms. Together these account for nearly all of the predicted photon absorption strength. Contributions from 3N photon absorption or from initial $(\gamma,\pi NN)$ processes are negligible. The 2N mechanism gives rise to a peak in the differential cross section at approximately $T_p = (E_\gamma - S_{2N})/2$, where S_{2N} is the two nucleon separation

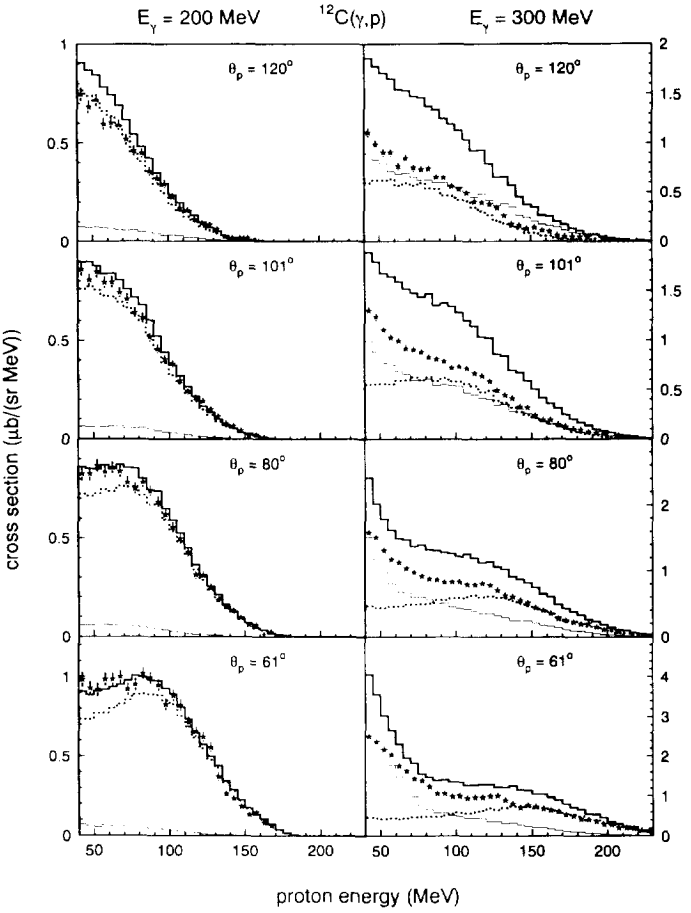

Fig. 4. The ^{12}C(γ,p) differential cross section as a function of proton energy compared with calculations using the Valencia model [13,14] for E_γ = 200 and 300 MeV. The dotted lines show the contributions from initial 2N photon absorption mechanisms. The thin solid lines show the contributions from initial (γ,πN) processes. The thick solid lines show the results of the full calculation, which includes 3N photon absorption and (γ,πNN) processes.

energy, whereas the strength of the QFπ mechanism is concentrated at lower proton energies. The magnitude of the 2N component falls and its width increases with increasing photon energy. It dominates the spectrum at E_γ = 200 MeV, but is almost totally suppressed at 500 MeV where the maximum intensity of the distribution is beyond the upper proton energy threshold. The (γ,πN) component is very weak at 200 MeV but rises to a maximum strength between 300 and 400 MeV before falling again. This distribution moves to higher proton energies with higher photon energy due to reaction kinematics. At $E_\gamma \geqslant 400$ MeV the (γ,πN) component dominates the predicted cross section.

At E_γ = 200 MeV, where 2N photon absorption is dominant, the agreement with the data is extremely good. This suggests that the calculation accounts well for the

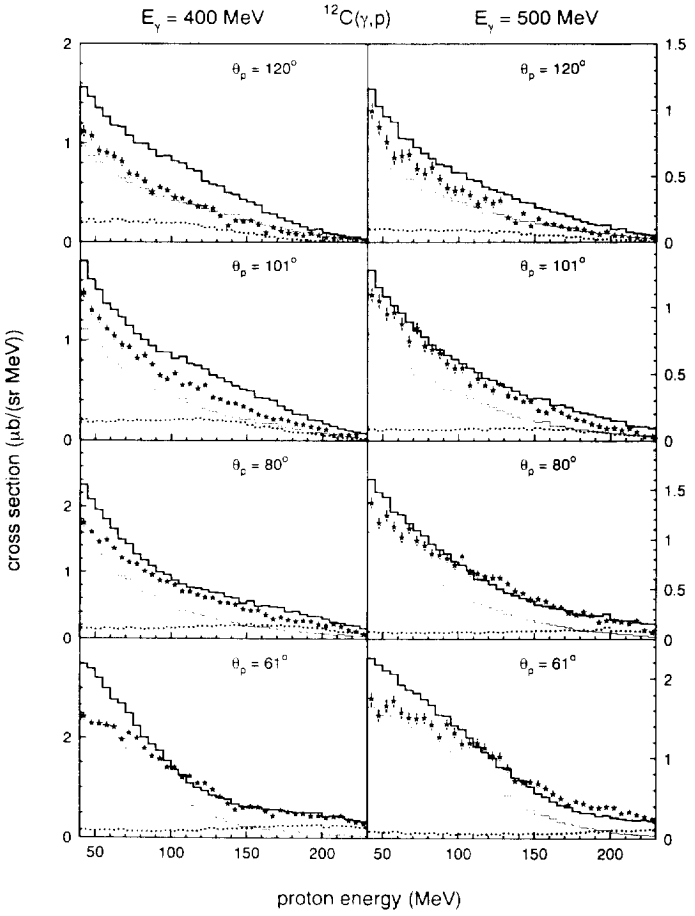

Fig. 5. As Fig. 4 for E_γ = 400 and 500 MeV.

2N absorption process. At higher photon energies the calculations predict reasonable shapes for the proton energy spectra, although the calculated cross sections have greater strength than the data. The differences are large at E_γ = 300 and 400 MeV, particularly at backward proton angles. At E_γ = 500 MeV the differences are much smaller, but the calculation does not include any two-pion production processes, which are expected to become important at this energy and which can contribute to the (γ,p) cross section through FSI.

At E_γ = 300 MeV the (γ,p) calculation predicts substantial strength for both the (γ,πN) and 2N photon absorption mechanisms at all proton angles. The magnitude of the (γ,πN) component decreases with proton angle, while the 2N component has a much weaker angular dependence with its maximum strength at proton angles between 61° and 80°. Both distributions move to smaller proton energies at large proton angles because of the reaction kinematics and the greatest distinction between the two processes is at the smallest proton angles. Although the calculations have greater strength than

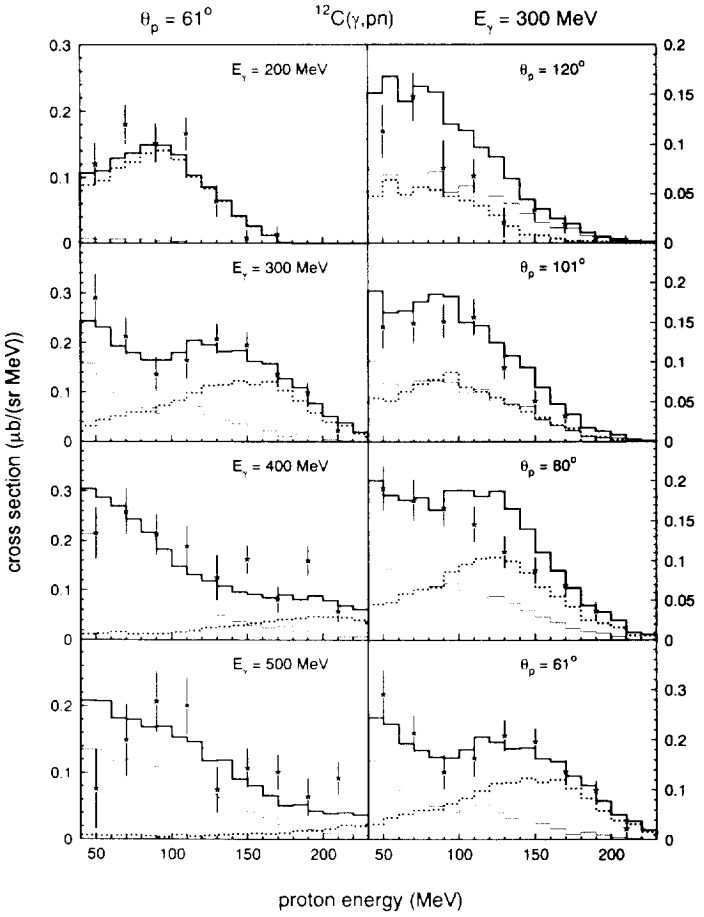

Fig. 6. The $^{12}C(\gamma,p)$ differential cross section as a function of proton energy, with the condition that a neutron is detected in TOF, compared with calculations using the Valencia model [13,14]. The lines have the same meaning as in Fig. 4.

the data at this energy it is clear that both mechanisms are necessary to account for the shapes of the measured spectra.

3.2.2. *Coincidence reactions*

Fig. 6 shows the measured and calculated differential cross sections as a function of proton energy with the condition that a coincident neutron is detected in TOF. The figure presents a selection of photon energies and proton angles illustrating the photon energy dependence of the reaction at $\theta_p = 61°$ and the angular dependence of the reaction at $E_\gamma = 300$ MeV. As in the exclusive (γ,p) reaction, 2N absorption and the $(\gamma,\pi N)$ mechanism (which contributes through FSI) account for nearly all of the reaction strength. Contributions from 3N photon absorption or from initial $(\gamma,\pi NN)$ processes are negligible. At 200 MeV the (γ,pn) reaction is dominated by 2N photon absorption.

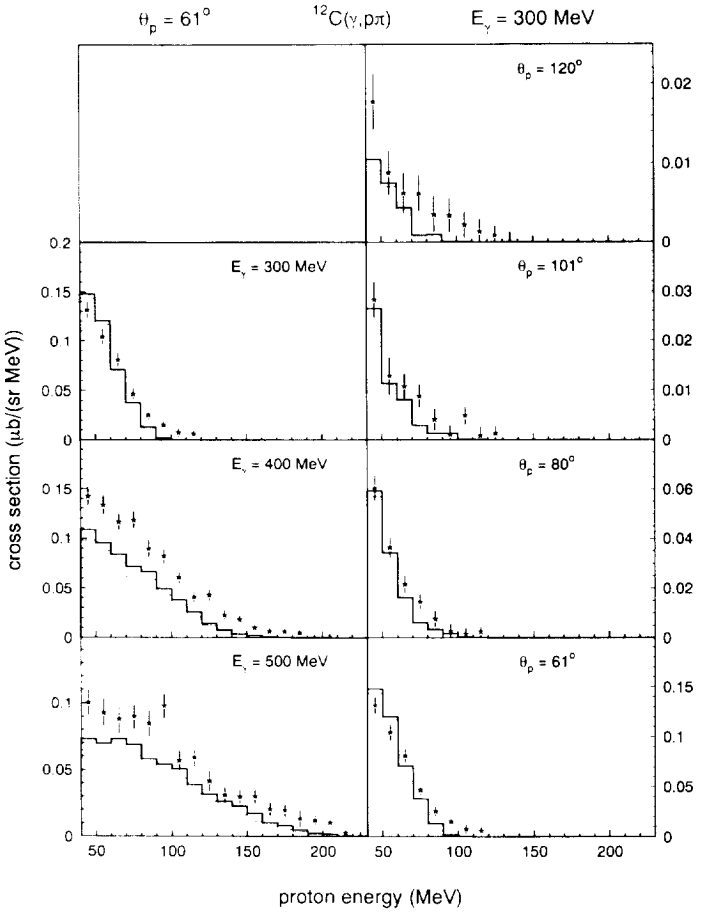

Fig. 7. The $^{12}C(\gamma,p)$ differential cross section as a function of proton energy, with the condition that a charged pion is detected in TOF, compared with calculations using the Valencia model [13,14]. The lines have the same meaning as in Fig. 4.

At 300 MeV there is strong competition from $(\gamma,\pi N)$ events and at higher photon energies the $(\gamma,\pi N)$ mechanism dominates. At all angles at 300 MeV the calculations predict comparable strengths for initial $(\gamma,\pi N)$ and 2N processes and, as in the case of the single-arm spectra, the shapes of these two major components become similar at backward angles.

The total calculated strength, and the calculated shapes of the proton energy spectra agree reasonably well with the data at all photon energies and all proton angles, although the calculated strength at E_γ = 300 MeV exceeds the data at backward angles.

Fig. 7 shows the differential cross section, for data in which a coincident charged pion is detected in TOF. However, it should be noted that the present detector geometry allows very few direct QFπ events to be observed. The $(\gamma,p\pi)$ reaction has no contribution from initial 2N or 3N photon absorption mechanisms in the Valencia model. Neither

does the model include any two-pion production mechanisms which may be important in this channel at high photon energies. Initial (γ,πN) processes dominate the predicted differential cross section, largely through final state rescattering, although there is a small contribution from (γ,πNN) processes at the highest photon energies. The calculations give the correct shape at all photon energies. The magnitude is in good agreement with the data at E_γ = 300 MeV, but is somewhat less than the data at higher photon energies. This may be due to the lack of two-pion production mechanisms in the calculations. The forward peaking of the (γ,πN) cross section is very clear in the proton angular dependence. Given the factor of $\sim$ 10 increase from backward to forward proton angles at E_γ = 300 MeV, the agreement between the calculation and the experimental data is very good at this energy.

The comparison for the (γ,pp) reaction is shown in Fig. 8. Direct photon absorption on proton–proton pairs is predicted to have a small cross section and large contributions arise from FSI following (γ,πN) or (γ,pn), and from 3N photon absorption. The calculations predict similar strengths arising from initial absorption on proton–proton and proton–neutron pairs but the contribution from initial absorption on proton–neutron pairs is concentrated at lower proton energies since half the detected protons necessarily arise through FSI. At 200 MeV these 2N absorption processes provide most of the strength, but the (γ,πN) strength dominates at higher energies, increasing to a maximum between 300 and 400 MeV. At photon energies $\geqslant$ 300 MeV there is a predicted contribution to the (γ,pp) channel from 3N photon absorption events (not shown), which is comparable in magnitude to the 2N absorption mechanisms.

The (γ,pp) data are smaller than the model predictions in all kinematic regions. Given the very large predicted contributions to this channel from QFπ absorption and FSI this lack of agreement is perhaps not surprising and one or both of these processes is clearly overestimated in the calculation. At E_γ = 200 and 300 MeV the calculated strength of direct absorption on proton–proton pairs is also greater than the data at forward proton angles. No definite conclusions about the contributing mechanisms can be drawn but it is clear that a large part of the cross section arises from two-step processes.

Overall the Valencia model accounts better for the coincidence data shown in Figs. 6–8 than for the single-arm spectra in Figs. 4 and 5. This situation is probably due to the incomplete coverage of the TOF detectors. As a result the single-arm spectra contain strength due to reactions in which one particle is at an angle, probably forward, not covered by TOF. The discrepancies between the single-arm data and the Valencia model shown in Figs. 4 and 5 may be due to such events.

In summary, the Valencia model has provided a good overall account of the general features of the measured data and has demonstrated that both 2N and QFπ photon absorption mechanisms are important in the photon energy range of these measurements. For the (γ,pp) channel, and in some kinematic regions for the other channels, it predicts too large a cross section, although it is not clear from the present analysis which mechanisms are too strong. One shortcoming of the model is that it contains no nuclear structure information and this may in future be a serious drawback for making detailed comparisons with particle momentum and missing energy distributions. In contrast, the

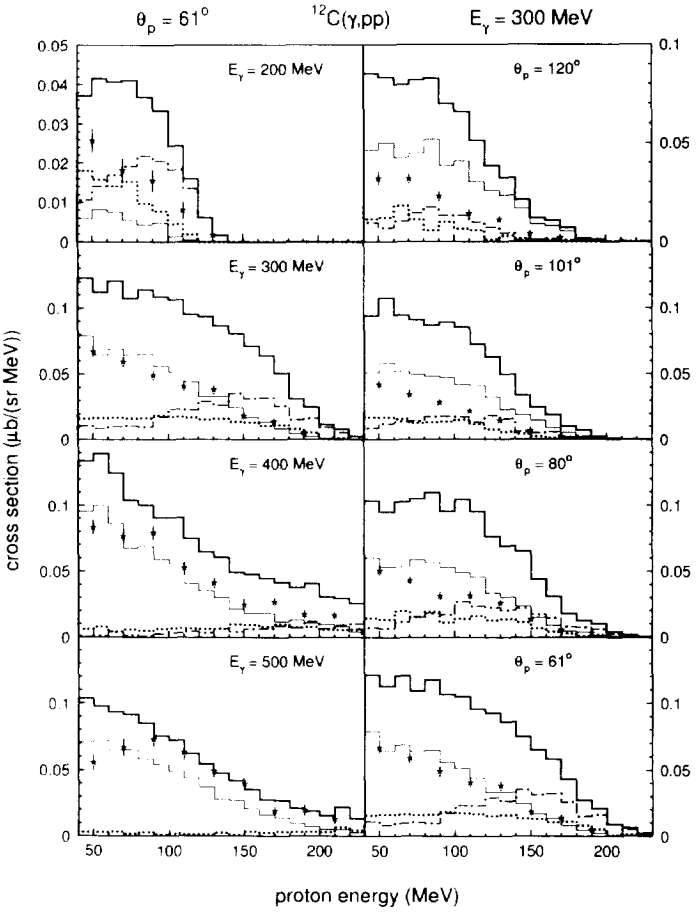

Fig. 8. The $^{12}C(\gamma,p)$ differential cross section as a function of proton energy, with the condition that a second proton is detected in TOF, compared with calculations using the Valencia model [13,14]. The dotted lines show the contributions from initial photon absorption on pn pairs. The dot-dash lines show the contributions from initial photon absorption on pp pairs. The thin solid lines show the contributions from initial $(\gamma,\pi N)$ processes. The thick solid lines show the results of the full calculation, which includes 3N photon absorption and $(\gamma,\pi NN)$ processes.

Gent group has carried out microscopic calculations of the basic (γ,pn) and (γ,pp) two-body knockout processes, which are presented in the next subsection. These calculations can in principle provide a better description of momentum and energy distributions. They are, however, much less complete than the Valencia calculations, since they do not include the important "indirect" processes arising from QFπ production followed by pion FSI.

3.3. Comparison with the Gent model

The Gent group has investigated the importance of microscopic two-body photon absorption mechanisms in the exclusive (γ,NN) [15] and semi-exclusive (γ,N) [16] reaction cross sections. The calculations are based on a shell model approach and use an unfactorised formalism which avoids many of the assumptions inherent in previous calculations of (γ,NN) processes. Even so, the model starts from a spectator picture and only two-body photoabsorption mechanisms are considered. This corresponds with the "direct" production of two nucleons in the Valencia model. The main difference between both approaches is that in the Gent model the elementary pion-exchange current operators are used in a finite nucleus calculation. None of the "indirect" production mechanisms, which were shown to be important in various parts of phase space, are considered in the Gent model. As these processes gain importance with increasing photon energy, the Gent calculations are limited to photon energies up to $\sim$ 300 MeV. In the Gent model, the basic photon absorption mechanisms include the so-called seagull and pion-in-flight exchange currents and the isobar current diagrams. The effects of FSI between the emitted nucleons and the residual core are calculated in a distorted partial wave approach, although the effects of interactions between the two emitted nucleons are neglected, the two particles being treated independently after the initial photonuclear interaction. The FSI treatment does not include multi-step processes such as charge exchange or final state scattering which could lead to the ejection of more than two nucleons.

The Gent calculations include the contribution of quasi-free pion production to the semi-exclusive (γ,p) channel. The pion production operators used in these calculations are shown to give a good account of the elementary γ+p$\rightarrow$N+π processes on a free proton [17]. However, the calculated (γ,pπ) contribution to the semi-exclusive (γ,p) channel does not account for either proton or pion FSI.

The calculations presented in Figs. 9–11 below were carried out for the geometry of the present detectors and provide a direct comparison with the present data.

3.3.1. The $^{12}C(\gamma,p)$ reaction

Fig. 9 shows the ^{12}C(γ,p) cross sections compared with the Gent model. The 2N calculation includes contributions from both the (γ,pn) and (γ,pp) photon absorption processes. At E_γ = 200 MeV the figure confirms that nearly all of the cross section arises from 2N photon absorption, as already suggested by comparison with the Valencia model. FSI between the outgoing nucleons and the residual nucleus do not dramatically distort the proton energy spectra calculated from 2N photon absorption but reduce their magnitude, producing agreement with the data and with the Valencia result for 2N photon absorption (dotted line). The calculated contribution from direct QFπ processes is small and concentrated at proton energies below 40 MeV. The overall agreement with the data is good, except at proton energies $\sim$ 50 MeV. The lack of strength at these energies is similar to differences previously observed [16] between ^{12}C(γ,p) data and the Gent model at lower photon energies. These differences are not evident in the comparisons

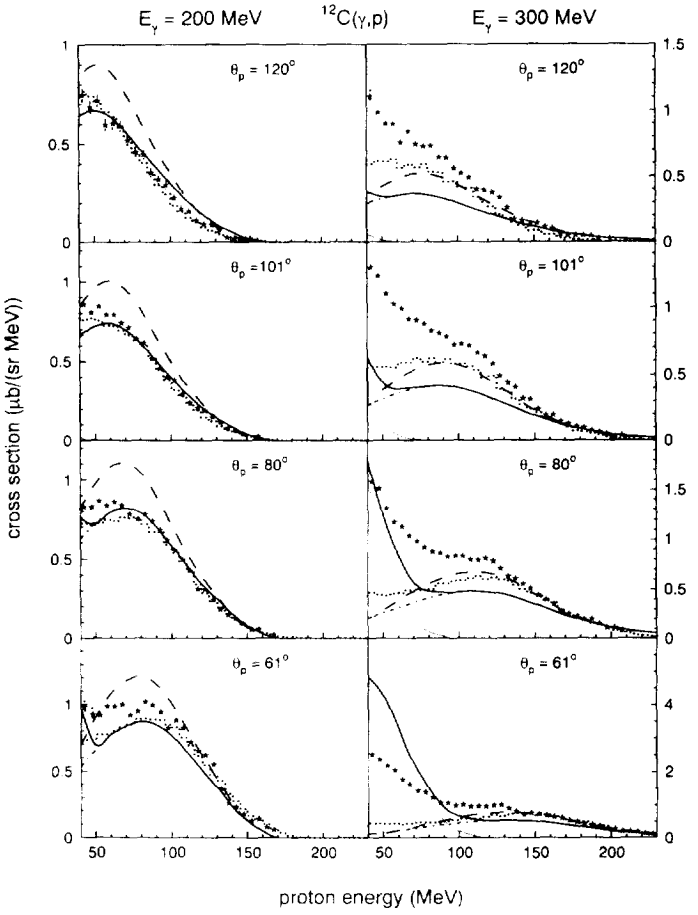

Fig. 9. The ^{12}C(γ,p) differential cross section as a function of proton energy compared with calculations using the Gent model. The dashed (dot-dashed) lines show the total contribution from (γ,pn) and (γ,pp) processes, without (with) FSI corrections. The thin solid lines show the contributions from (γ,pπ) processes, without FSI corrections for either the protons or the pions. The thick solid lines show the sum of both of the (γ,2N) processes (with FSI) and the (γ,pπ) processes (without FSI). For comparison the dotted line shows the contribution from initial photon absorption on 2N pairs, calculated using the Valencia model.

with the total differential cross sections calculated using the Valencia model shown in Fig. 4, which suggests that they are due the effects of final state pion rescattering or reabsorption not included in the Gent model.

At E_γ = 300 MeV the agreement between the data and the total calculated strength is rather poor. This is consistent with the conclusion reached in the previous subsection that initial pion production followed by rescattering is increasingly important at photon energies $\geqslant$ 300 MeV. Without such FSI the Gent model cannot be expected to account for all of the observed strength especially at low proton kinetic energies and forward angles. At the highest proton energies, where two-step processes are suppressed and 2N photon absorption mechanisms are expected to dominate, there is reasonable agreement.

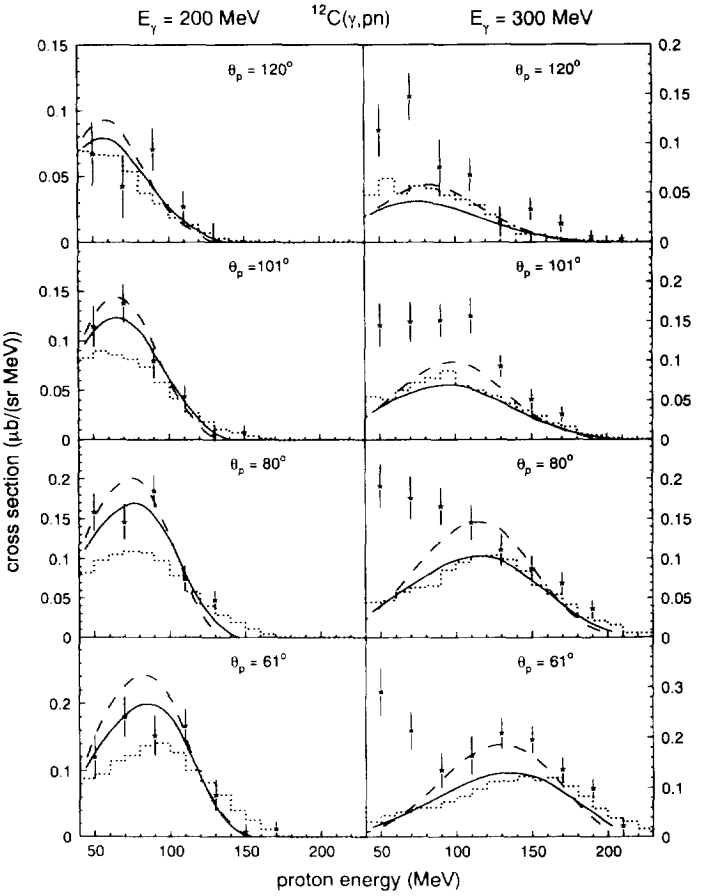

Fig. 10. The ^{12}C(γ,p) differential cross section as a function of proton energy, with the condition that a neutron is detected in TOF, compared with calculations using the Gent model. The dashed (solid) lines show the contributions from (γ,pn) processes, without (with) FSI corrections. For comparison the dotted line shows the contribution from initial photon absorption on 2N pairs, calculated using the Valencia model.

A comparison of the 2N calculated strength with the Valencia model shows that the shapes are almost identical although the magnitudes predicted by the Gent model are somewhat smaller than the Valencia model, particularly at backward proton angles, where the total differential cross section calculated in the Valencia model exceeds the data.

3.3.2. Coincidence reactions

The comparisons in Fig. 10 between the ^{12}C(γ,pn) cross sections and the Gent model confirm the conclusions of the previous subsection. At $E_\gamma = 200$ MeV the data are very well described by the Gent model (γ,pn) photon absorption calculation. The effects of FSI on the two outgoing nucleons are relatively small and their main effect is to reduce the differential cross section at lower proton energies, improving the agreement with the

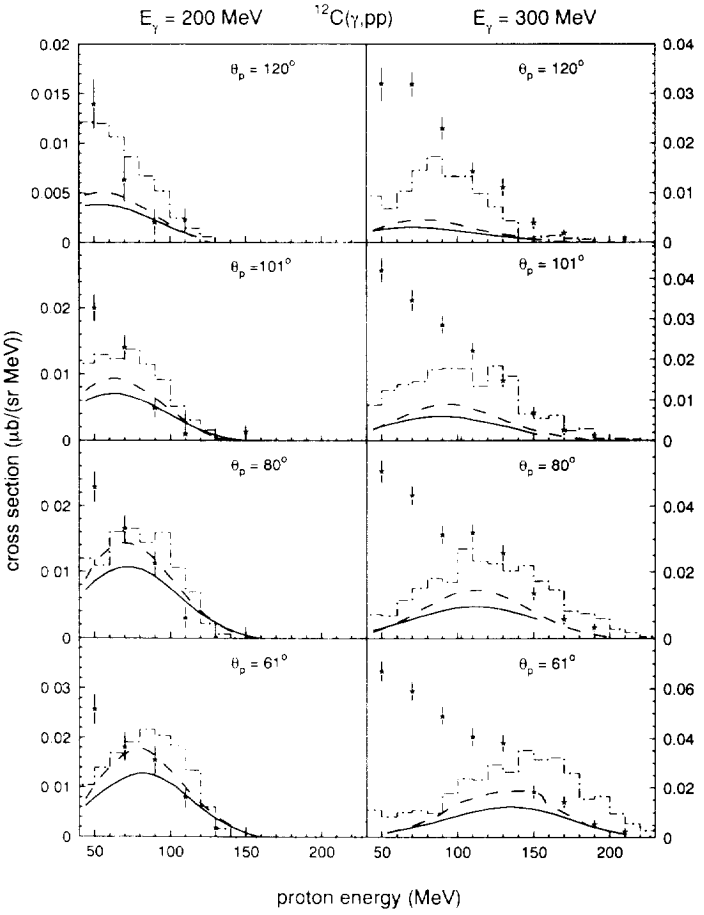

Fig. 11. The ^{12}C(γ,p) differential cross section as a function of proton energy, with the condition that a proton is detected in TOF, compared with calculations using the Gent model. The dashed (solid) lines show the contributions from (γ,pp) processes, without (with) FSI corrections. For comparison the dot-dashed line shows the contribution from initial photon absorption on pp pairs, calculated using the Valencia model.

data. At E_γ = 300 MeV the data are not so well described. The effects of FSI of the outgoing nucleons are again relatively small but overall the calculations only account for about half of the measured differential cross section and the remainder can be attributed to the (γ,Nπ) interaction followed by FSI. The agreement with the data gets better at higher proton energies where the contribution from this two-step mechanism is smaller. Comparing the Gent and Valencia model predictions of 2N photon absorption, it is evident that the overall agreement between both models is remarkably good. Both predict similar spectrum shapes, although relatively small differences in magnitude are seen at E_γ = 200 MeV.

Fig. 11 shows the ^{12}C(γ,pp) data compared to calculations of direct photon absorption on proton–proton pairs carried out using the Gent model. The calculated (γ,pp) strength is much weaker than the corresponding (γ,pn) strength. At both photon en-

ergies the calculated cross sections are much smaller than the data, particularly at lower proton energies, confirming the importance of the two-step processes not included in the calculation. At the highest proton energies, where these processes have little strength, the calculations give better agreement with the data. The Gent (γ,pp) calculations are also compared with the component of the Valencia model arising from initial photon absorption on proton–proton pairs. The shapes predicted by both models are similar, although the Valencia model predicts a consistently greater cross section.

4. Conclusions

Data on the photoproduction of protons from ^{12}C have been obtained at four photon energies in the range 200–500 MeV and have been presented as partial differential cross sections as a function of proton energy for both the inclusive (γ,p) reaction and for the coincident (γ,pn), (γ,pp) and (γ,pπ) reactions.

Reasonable agreement is obtained with the inclusive ^{12}C(γ,p) cross section measurements at Tokyo and Frascati, but the present single-arm cross sections are smaller than those measured at Bonn, especially at forward proton angles. Comparisons with the Bonn coincidence cross sections for ^{16}O give much better agreement with the present ^{12}C data once differences in the target and geometry have been taken into account.

The data are compared to two current microscopic models of the photon absorption process. The comparison with the Valencia model shows that it is possible to account for the general trends of the data in terms of two initial photon absorption mechanisms, quasi-free pion production and photon absorption by correlated nucleon pairs as long as the effects of FSI are taken into account. The (γ,p) channel agrees in both shape and magnitude with the calculations at E_γ = 200 MeV where 2N photon absorption dominates. At higher energies, where quasi-free pion production dominates, the model agrees in shape with the data, but overestimates the magnitude of the cross sections. There is reasonably good agreement between the present data and the model for the (γ,pn) channel at all photon energies and proton angles. The (γ,pπ) data are well described by the model at E_γ = 300 MeV, but at higher photon energies the calculations fail to reproduce the measured strength. This may be due to two-pion production processes not included in the calculations. The weak (γ,pp) channel, which the calculations suggest is dominated by FSI, is accounted for rather poorly by the calculations.

Comparison of the present data with the Gent model, which stresses the 2N absorption aspects of the reactions under study, shows good agreement at E_γ = 200 MeV for the (γ,p) and (γ,pn) data. At E_γ = 300 MeV good agreement is observed at high proton energies, but the lack of agreement at lower proton energies indicates the need for multi-step processes in these channels. At both photon energies the calculations of the (γ,pp) cross sections greatly underestimate the data, especially at low proton energies. This missing strength is again likely to be due to multi-step processes which are not included in the calculations.

The few previous (γ,2N) or (γ,Nπ) coincidence experiments performed in the Δ-resonance region [5–9,27,28] have too little angular or energy coverage or insufficient energy resolution to allow a detailed analysis of the correlations between the two ejected particles. This information is required to provide an accurate assessment of the integrated QD and QFπ cross sections and to estimate their relative contributions to the total photon absorption cross section in the Δ-resonance region. While the present work has provided insight into the main photoproduction processes at intermediate energies, it is clear that much more information about the constituent reaction mechanisms will be forthcoming from detailed analyses of the energy and angular correlations between the emitted particles in the (γ,NN) channels. Such analyses, making use of data at all photon energies, are currently under way and will be published later.

Acknowledgements

This work was supported by the UK Science and Engineering Research Council, the British Council, the Deutsche Forschungsgemeinschaft (Mu 705/3), BMFT (06 Tü 656), DAAD (313-ARC-VI-92/118), the European Community (SCI.0910.C(JR)) and NATO (CRG 920171). The authors would like to thank the Institut für Kernphysik der Universität Mainz for the use of its facilities and for the generous assistance provided during the course of this experiment. We are indebted to Prof. E. Oset for allowing us to use the Valencia photoproduction code and for useful discussions on its interpretation. Two of us (GEC and JAM) would like to thank the SERC for financial support in the form of research studentships during the period of this work.

References

[1] S.N. Dancer et al., Phys. Rev. Lett. 61 (1988) 1170.
[2] S.M. Doran et al., Nucl. Phys. A 559 (1993) 347.
[3] I.J.D. MacGregor et al., Nucl. Phys. A 533 (1991) 269.
[4] J.C. McGeorge et al., Phys. Rev. C 51 (1995) 1967.
[5] J. Arends et al., Z. Phys. A 298 (1980) 103.
[6] J. Arends et al., Nucl. Phys. A 526 (1991) 479.
[7] S. Homma et al., Phys. Rev. C 27 (1983) 31.
[8] M. Kanazawa et al., Phys. Rev. C 35 (1987) 1828.
[9] K. Baba et al., Nucl. Phys. A 415 (1984) 462; Phys. Lett. B 113 (1982) 459.
[10] M. Anghinolfi et al., Nucl. Phys. A 457 (1986) 645.
[11] I. Anthony et al., Nucl. Instr. Meth. A 301 (1991) 230.
[12] H. Herminghaus et al., Nucl. Instr. Meth. A 138 (1976) 1; A 187 (1981) 103.
[13] R.C. Carrasco and E. Oset, Nucl. Phys. A 536 (1992) 445.
[14] R.C. Carrasco, M.J. Vicente Vacas and E. Oset, Nucl. Phys. A 570 (1994) 701.
[15] J. Ryckebusch et al., Nucl. Phys. A 568 (1994) 828.
[16] J. Ryckebusch et al., Phys. Rev. C 49 (1994) 2704.
[17] M. Vanderhaegen et al., submitted for publication.
[18] I.J.D. MacGregor, Proc. Workshop on Future detectors for photonuclear experiments, Edinburgh, May 1991, ed. D. Branford (1992) p. 232;
I.J.D. MacGregor et al., to be published.

[19] P. Grabmayr et al., Proc. Workshop on Future detectors for photonuclear experiments, Edinburgh, May 1991, ed. D. Branford (1992) p. 225.
[20] I.J.D. MacGregor et al., Nucl. Instr. Meth. A 262 (1987) 347.
[21] J.R.M. Annand, I. Anthony and A.H. Sibbald, University of Glasgow internal report (1994), to be published.
[22] D.F. Measday and C. Richard-Serre, CERN report 69-17 (1969).
[23] R.A. Cecil, B.D. Anderson and R. Madey, Nucl. Instr. Meth. A 161 (1979) 439.
[24] P. Rossi et al., Phys. Rev. C 40 (1989) 2412.
[25] D.A. Jenkins, P.T. Debevec and P.D. Harty, Phys. Rev. C 50 (1994) 74.
[26] E. Oset, private communication.
[27] I.V. Glavankov and V.N. Stibunov, Sov. J. Nucl. Phys. 30 (1979) 465;
I.V. Glavankov, Sov. J. Nucl. Phys. 49 (1989) 58;
P.S. Anan'in and I.V. Glavankov, Sov. J. Nucl. Phys. 52 (1990) 205.
[28] L.D. Pham et al., Phys. Rev. C 46 (1992) 621.